Available online at www.sciencedirect.com
ScienceDirect
Trans. Nonferrous Met. Soc. China 35(2025) 362−376
Transactions of Nonferrous Metals Society of China
www.tnmsc.cn

Influence of high-temperature and short-time solution treatment on microstructure and properties of Al−Mg−Zn−Ag alloy

Cheng GUO[1], Yi-fei CHEN[1], Yu-qin GUO[1], Huan WANG[1], Hai-tao ZHANG[2], Jing-qi CHEN[1], Zi-bin WU[3], Xin-gang LIU[1], Hiromi NAGAUMI[3]

1. School of Mechanical Engineering, Yanshan University, Qinhuangdao 066004, China;
2. Key Lab of Electromagnetic Processing of Materials, Ministry of Education, Northeastern University, Shenyang 110004, China;
3. High-Performance Metal Structural Materials Research Institute, Soochow University, Suzhou 215021, China

Received 5 July 2023; accepted 29 February 2024

Abstract: High-temperature and short-time (HTST) solution heat treatment combined with non-isothermal aging (NIA) was employed to regulate the microstructure and properties of Al−4.5Mg−2.0Zn−0.3Ag alloy. Results indicate that HTST solution heat treatment can not only retain partial deformation dislocations, but inhibit the recrystallization behavior and increase the proportion of low-angle grain boundaries (LAGBs). In the subsequent NIA process, HTST solution heat treatment combined with NIA is instrumental in restraining the degradation of dislocations and promoting precipitation of nano-scale T'-$Mg_{32}(Al,Zn,Ag)_{49}$ phase, which improves the strength of the alloy greatly. In addition, a higher fraction of LAGBs and the discontinuous distribution of grain boundary precipitates caused by this novel technology meliorate the corrosion resistance of Al−4.5Mg−2.0Zn−0.3Ag alloy.

Key words: Al−Mg−Zn−Ag alloy; solution treatment; non-isothermal aging; microstructure; mechanical properties; corrosion resistance

1 Introduction

In recent years, the reduction of carbon emissions has increasingly become the focus of attention. Correspondingly, the lightweight process in the field of traffic and transportation is becoming more and more urgent [1,2]. The development of lightweight materials is crucial to the reduction of carbon emissions [3,4]. In marine transportation, 5xxx aluminum alloy has always been the first choice for lightweight materials because of its weldability and nice corrosion resistance [5−7]. Nevertheless, the mechanical properties of 5xxx aluminum alloys are suppressed owing to the ascription of non-heat-treatment [8]. Some methods that can enhance the strength of alloys, such as solution strengthening and work hardening, cause the deterioration of corrosion resistance [9−11]. Thus, it is an urgent problem to enhance the mechanical properties of 5xxx aluminum alloy on the premise of ensuring its good corrosion performance.

In recent studies, improving the age-strengthening mechanism of 5xxx aluminum alloy by alloying is an effective path to develop novel high-strength 5xxx aluminum alloys with good corrosion resistance [12−14]. HOU et al [15] modified the composition of 5xxx alloy with 2.0−3.0 wt.% Zn, resulting in the formation of nano-scale T-$Mg_{32}(Al,Zn)_{49}$

Corresponding author: Cheng GUO, Tel: +86-335-8074783, E-mail: chengguo@ysu.edu.cn;
Xin-gang LIU, Tel: +86-335-8072380, E-mail: lxg@ysu.edu.cn
DOI: https://doi.org/10.1016/S1003-6326(24)66685-9

phase and improving the aging-hardening response. Applying minor amount of Cu is also an efficient way to increase the strength of 5xxx aluminum alloys by the *S*-Al_2MgCu phase and its precursors [16,17]. In addition, the alloying of Ag can increase the corrosion performance and mechanical properties of 5xxx aluminum alloy [18]. To reduce the cost of the alloy, in our previous studies, the composite microalloying of Ag and Zn plays a positive effect on increasing the corrosion performance and mechanical properties of 5xxx aluminum alloy [19]. This novel Al−Mg−Zn−Ag alloy with competitive mechanical properties and corrosion performance is of great significance to the lightweight in marine transportation.

For heat-treatable aluminum alloys, solution heat treatment is vital to the microstructure, mechanical properties as well as corrosion resistance [20,21]. One the one hand, solution heat treatment influences the content of alloying elements in solid solution, subsequently affecting the precipitation of nano-scale particles in the age-hardening step [22]. On the other hand, the solution heat treatment regulates the recovery and recrystallization behavior of grains in the as-quenched alloys, as well as the degradation and diffusion of dislocations, so as to improve the properties of the alloy. Although many studies have been conducted on conventional heat-treatable aluminum alloy systems (2xxx, 6xxx, and 7xxx aluminum alloys) [20−23], the influence of solution heat treatment on the novel heat-treatable 5xxx alloys has been reported rarely. Besides, non-isothermal aging (NIA) is an effective method to promote precipitation behavior with varying heating temperatures [24]. Nucleation and phase transition of heat-treatable aluminum alloy treated by NIA have also been reported in recent studies [25].

To regulate the microstructure and improve the mechanical properties as well as corrosion resistance of the Al−4.5Mg−2.0Zn−0.3Ag alloy, we proposed a novel technology of high-temperature and short-time (HTST) solution heat treatment combined with NIA. Under the action of this technology, multiscale microstructure, high strength, and corrosion resistance can be obtained. The investigation provides new ideas and theoretical guidance for high-performance aluminum alloys.

2 Experimental

2.1 Materials and procedures

The Zn and Ag bearing 5xxx alloy was prepared by copper mold casting at 720 °C. The chemical composition of the alloy is presented in Table 1. Alloy ingot rectangular in shape was homogenized at 470 °C for 24 h, and rolled to 5 mm at 420 °C. After that, the plate was cold-rolled to 2 mm with a thickness reduction of 60%. Then, a series of solution heat treatments (480 °C, 1 h; 480 °C, 30 min; 500 °C, 10 min) were employed followed by water quenching. Subsequently, all of them were subjected to a NIA treatment, heating from room temperature (about 20 °C) to 220 °C with a heating rate of 10 °C/h. Detail schematic diagram of the solution−aging processing routes is shown in Fig. 1.

Table 1 Compositions of investigated alloy (wt.%)

Alloy	Mg	Zn	Ag	Mn	Fe	Al
Designed	4.5	2.0	0.3	0.5	0.1	Bal.
Actual	4.4	1.9	0.3	0.5	0.1	Bal.

2.2 Corrosion testing and electrochemistry measurement

The intergranular corrosion (IGC) resistance was evaluated by immersion tests according to GB/T 7998—2005. The dimensions of each sample were 40 mm (RD) × 25 mm (TD) × 2 mm (ND). Samples were immersed in corrosion solution (30 g NaCl + 10 mL HCl + 1 L deionized water) at 35 °C for 24 h. After immersion, the corrosion depth was evaluated by OM (ZEISS Axio Imager M2m) on the transverse section (ND × TD). The corrosion morphologies at the rolling front (RD × TD) of corroded samples were characterized by SEM (ZEISS Sigma 300) and confocal laser scanning microscope (CLSM, OLYMPUS LEXT OLS4000). A detailed schematic diagram of testing samples is shown in Fig. 2.

An electrochemical workstation (CORRTEST CS310M) was employed for the measurement of polarization curves and electrochemical impedance spectra (EIS). The surface size of samples was 1.0 cm^2 and the aqueous solution was 3.5 wt.% NaCl. A platinum sheet was used for the counter electrode (CE) and the saturated calomel electrode

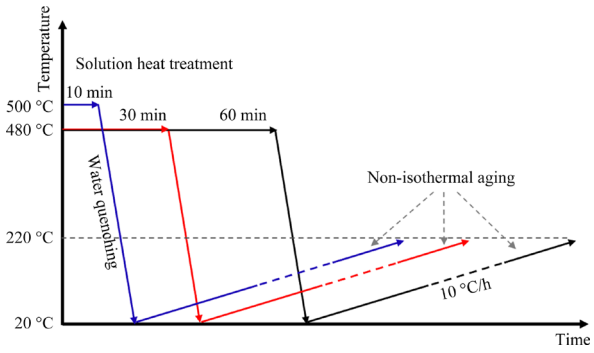

Fig. 1 Schematic diagram of solution-aging routes for investigated alloys

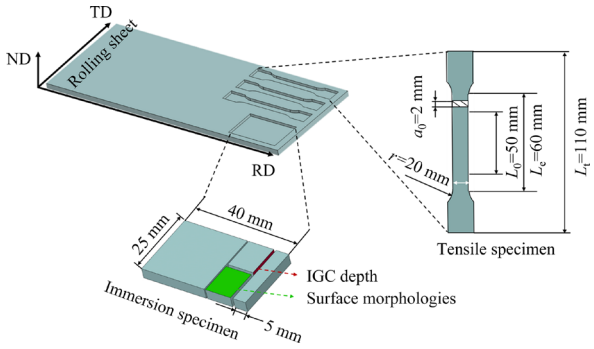

Fig. 2 Schematic diagram of tensile and immersion specimens machined from rolling sheet

(SCE) was the reference electrode. The EIS was measured at the voltage amplitude of 5 mV with a frequency of 100 kHz−100 mHz. ZSimpWin software was employed to fit EIS results. Polarization curves were acquired at a rate of 2 mV/s. At least five replicate tests were performed to guarantee reliability.

2.3 Measurement of hardness and mechanical properties

A hardness instrument (Qness, Q10A+) was employed to measure the hardness of investigated alloys. The loading was 4.9 N and the loading time was 10 s. Each sample was measured seven times and its average value was calculated. Mechanical properties were measured by tensile tests using a CSS−44100 type testing machine. Tensile tests were conducted with an initial strain rate of 6×10^{-4} s^{-1}, according to the GB/T16865—2013. Detailed dimensions of tensile test samples are shown in Fig. 2. Three parallel tests were conducted to ensure reliability.

2.4 Microstructure characterization

The microstructure of the as-quenched and as-aged alloys was characterized by SEM (ZEISS Sigma 300, 5 kV) equipped with an EBSD detector, and TEM (Talos F200S, 200 kV) with EDS analysis. Samples for the EBSD measurements were mechanically polished using SiO_2 suspension (3 and 0.02 μm) after abrading by SiC sandpapers (320#, 600#, 1000#, and 2000#). After that, samples were prepared via electrochemical polishing in the solution of $V(HClO_4):V(C_2H_5OH)$=1:9 for 30 s at a voltage of 25 V. Aztec Crystal software was employed for the data analysis. TEM specimens were twin jet electro-polished in the electrolyte of HNO_3 (30 vol.%) + CH_3OH (70 vol.%) at −25 °C and a voltage of 20 V.

3 Results and discussion

3.1 Microstructure of as-quenched alloys

Figure 3 shows SEM images of as-quenched alloys by different solution heat treatments. The microstructure of as-quenched alloys consists of coarse eutectic phases (marked by black arrows) and dispersed fine-scale precipitates (indicated by red arrows), as represented in Figs. 3(a−f). The corresponding EDS results in Fig. 3(g) indicate the major elements of Fe and Mn bearing in the coarse phases, and can be determined as $Al_6(Mn,Fe)$ which is transformed from $Al_6Mn + Al_{13}Fe_4 \rightarrow Al_6(Mn,Fe)$ during the solidification process [26].

To elucidate the fine-scale precipitates (red arrows in Figs. 3(d−f)), as well as clarify the dissolution behavior of solute atoms by different solution heat treatments, TEM images and corresponding EDS results of the as-quenched alloys are presented in Fig. 4. When the alloys are treated at 480 °C for 1 h (Fig. 4(a)) and for 30 min (Fig. 4(b)) followed by water quenching, the microstructure of alloys consists of diffuse Al_6Mn with the size of hundreds of nanometers. EDS-mapping results (Fig. 4(e)) show clear aggregation of Mn element with slight segregation of Fe. The component analysis in Fig. 4(f) reflects the difference in composition of the fine-scale precipitates and coarse eutectic phases (Fig. 3(g)). However, when the alloy was heated at 500 °C for 10 min followed by water quenching, the microstructure contains not only diffuse precipitates,

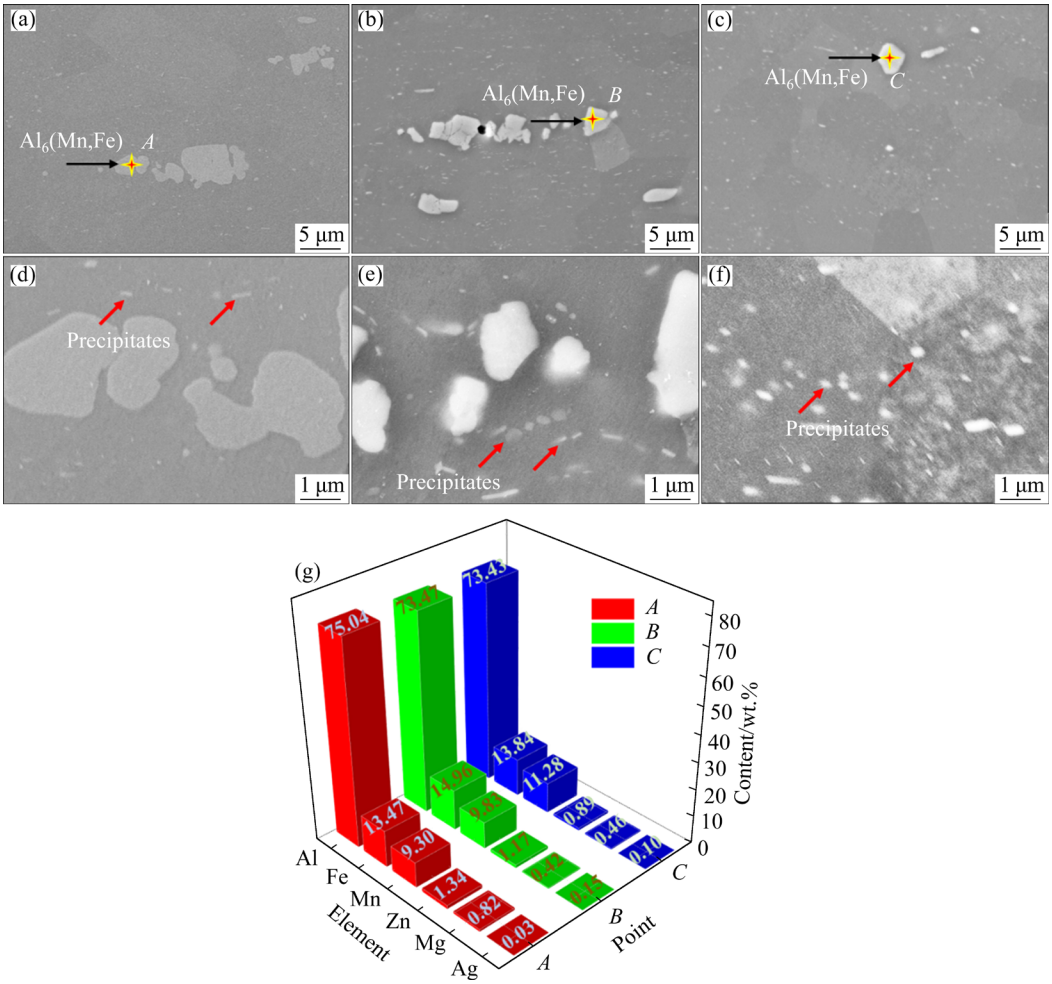

Fig. 3 SEM images of as-quenched alloys by solution heat treatments of 480 °C, 1 h (a, d), 480 °C, 30 min (b, e) and 500 °C, 10 min (c, f), and EDS results of analysis points *A*, *B*, and *C* labeled in (a−c), respectively (g)

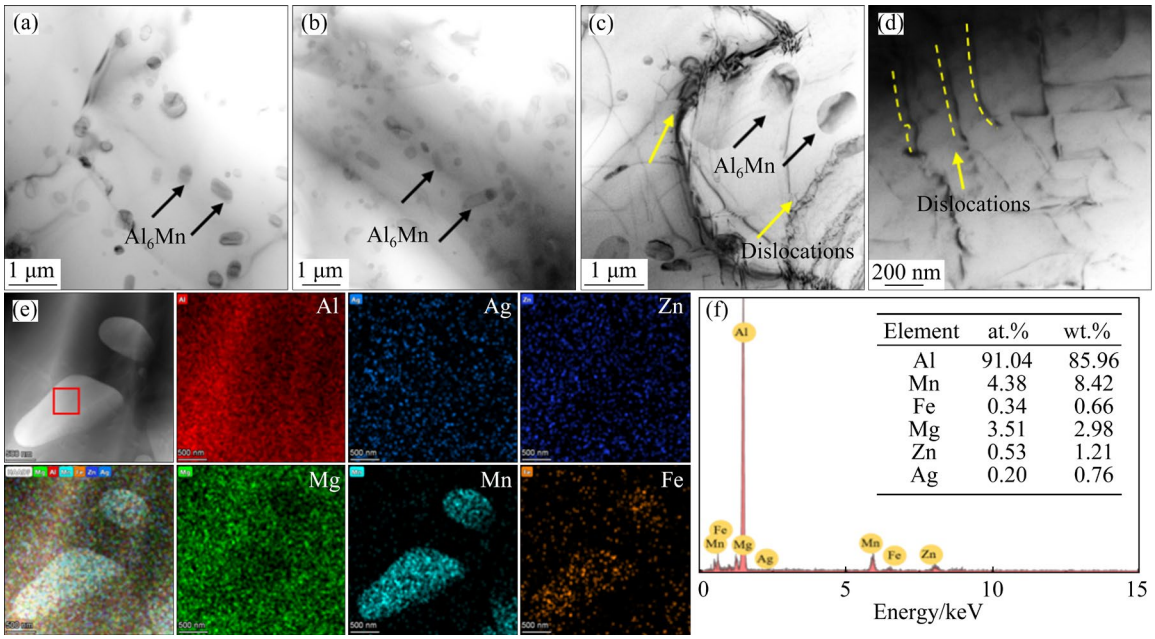

Fig. 4 TEM images of as-quenched alloys by solution heat treatments of 480 °C, 1 h (a), 480 °C, 30 min (b) and 500 °C, 10 min (c, d), and EDS results of precipitates (e, f)

but some residue dislocations, as shown in Figs. 4(c) and (d). These remain dislocations can serve as nucleation sites, so as to elevate the precipitation of nano-particles during aging treatment. Besides, due to the low aging temperature following NIA, dislocations can be maintained to improve the work hardening of the alloy.

According to the TEM images and EDS-mapping results, elements of Mg, Zn, and Ag of each as-quenched alloy are dissolved in the matrix completely. The results indicate that the investigated three solution technologies are all able to ensure the dissolution of the main alloy elements. However, only for alloy treated at 500 °C for 10 min, the cold rolling dislocations can be remainder. This also reflects the positive regulation of HTST solution heat treatment on the microstructure of the as-quenched alloy.

3.2 Evolution of hardness during NIA

After solution heat treatment, NIA with a heating rate of 10 °C/h is employed to promote the precipitation of strengthening phases. The evolution of hardness during NIA is shown in Fig. 5. During NIA, hardness shows a decreasing trend at the early aged stage, and then ascends rapidly with the prolonging of aging time and aging temperature. After solution heat treatment at 480 °C for 1 h, the alloy reaches the peak hardness value of HV (139.8±1.5) (denoted by S1 alloy) when aged for 16 h. When the time of solution heat treatment shortens to 30 min, the alloy reaches the peak hardness value of HV (137.5±2.3) (denoted by S2 alloy) as aged for 18 h. For the alloy solution treated at 500 °C for 10 min, the peak hardness of the alloy reaches HV (145.2±2.5) (denoted by S3 alloy), which is higher than that of other alloys. The results also reflect that a higher hardness is obtained with the HTST solution heat treatment followed by NIA.

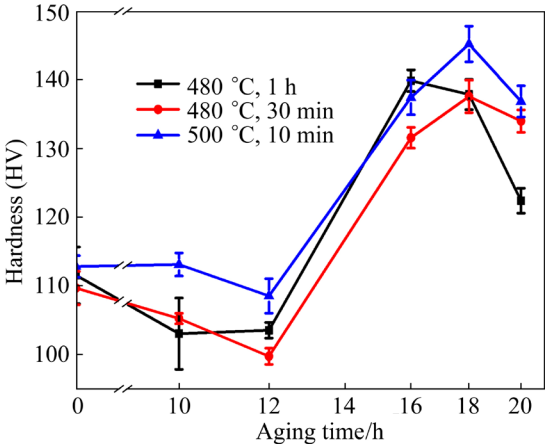

Fig. 5 Evolution of hardness of investigated alloys during NIA

3.3 Corrosion behavior of peak-aged alloys

3.3.1 IGC resistance and corrosion morphology

IGC resistance of peak-aged alloys is evaluated by immersion tests and corresponding cross-sectional (ND × TD) observations are shown in Fig. 6. The maximum IGC depths of S1, S2, and

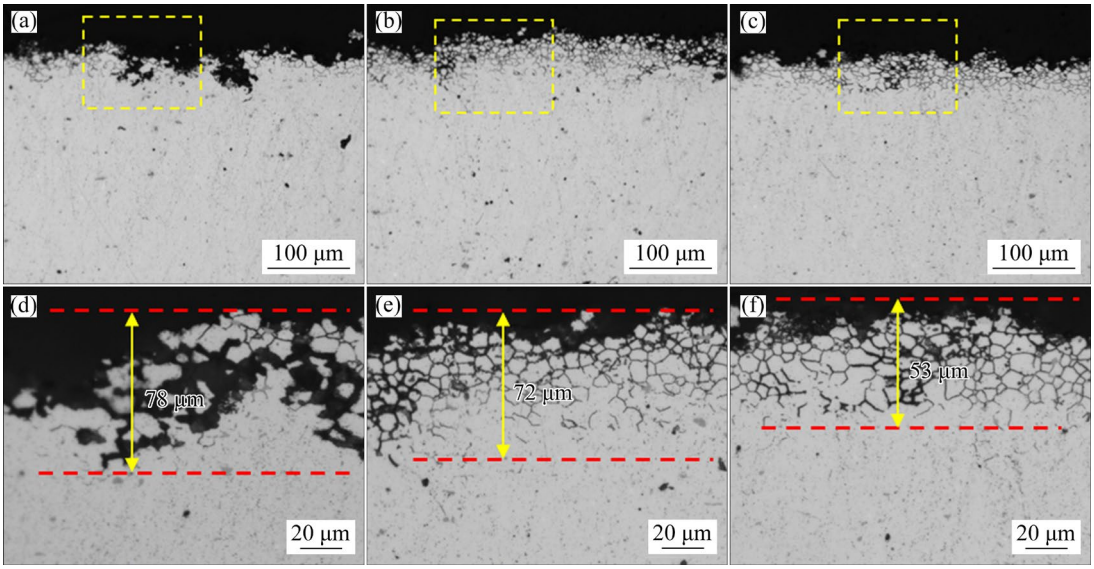

Fig. 6 (a−c) Typical cross-sectional (ND × TD) images of S1, S2 and S3 alloys, respectively; (d−f) Enlarged images of yellow dashed area in (a−c), respectively

S3 alloys are 78, 72 and 53 μm, respectively. This reflects that the S3 alloy with HTST solution heat treatment has better corrosion resistance than other peak-aged alloys.

To further clarify the corrosion behavior of the investigated alloys, 3D CLSM and SEM images of the surface (RD × TD) of immersed specimens are shown in Fig. 7. For the S1 alloy aged for 16 h, some deep corrosion areas (black dashed circles in Fig. 7(a)) can be observed. The maximum depth of the corrosion area is 86.7 μm. The corresponding microscopic morphology (Fig. 7(b)) shows an obvious outline of equiaxial grains (yellow dashed lines). Meanwhile, attacked grains (black arrows) and continuously attacked grain boundaries (red dashed lines) are also observed. This corrosion morphology indicates the sensitive intergranular corrosion performance of the alloy.

The microscopic morphology of the S2 alloy (aged for 18 h) is similar to that of S1 alloy, while the maximum depth of the corrosion area is 117.3 μm, as shown in Figs. 7(c, d). Nevertheless, for S3 alloy (aged for 18 h) with higher solution temperature and shorter solution time, the corroded surface is more uniform with the maximum depth of 70 μm (Fig. 7(e)). The microscopic morphology in Fig. 7(f) presents many exfoliated debris while attacked grain boundaries can be observed barely. The corrosion behavior of this alloy is prone to occur and penetrate along the Al-matrix rather than grain boundaries. This indicates that the HTST solution heat treatment is helpful for improving the corrosion resistance of grain boundaries.

3.3.2 Electrochemical behavior

Figure 8 shows potentiodynamic polarization curves of peak-aged alloys. The anodic branch presents an evident passivation stage, which demonstrates the positive role of oxide film on corrosion performance [27]. Comparing the corrosion potential (φ_{corr}) of the three alloys, S3 alloy represents higher φ_{corr} than the other two investigated alloys, which implies better corrosion performance of S3 alloy.

To further elucidate the corrosion mechanism of the peak-aged alloys, the electrochemical impedance spectra (EIS) of the alloys are depicted

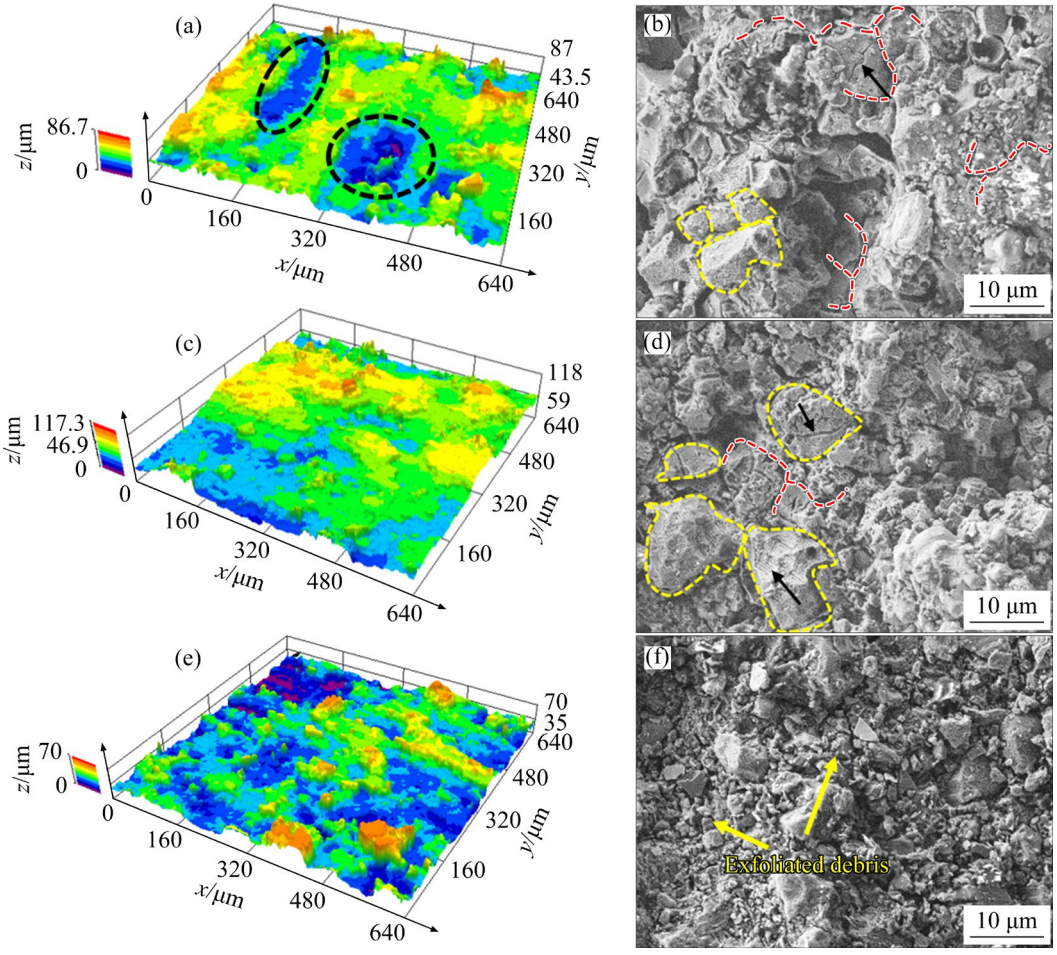

Fig. 7 3D CLSM and SEM images of corroded surfaces of S1 alloy (a, b), S2 alloy (c, d), and S3 alloy (e, f)

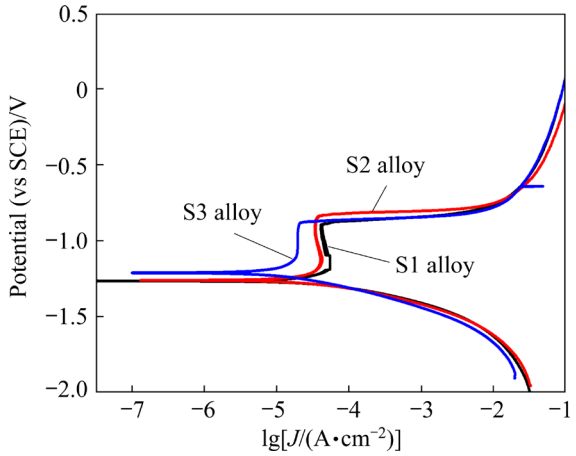

Fig. 8 Potentiodynamic polarization curves of peak-aged alloys

in Fig. 9(a). For S1 and S2 alloys, the impedance diagrams contain a higher-frequency capacitive loop and a lower-frequency inductance loop. The interface ions like Al^{3+} and O^{2-} induce charge transfer, which explains the formation of a higher frequency capacitive loop [28]. The lower frequency inductance loop is due to the reaction of Al^{3+} [29−31].

For S3 alloy, the impedance spectrum is composed of a higher-frequency capacitive loop and a lower-frequency capacitive loop. The formation of the higher frequency capacitive loop can also be explained by the resistance of charge transfer. Nevertheless, the lower frequency capacitive loop indicates no breach of oxide film during immersion, which also reflects the protective role of the oxide film on corrosion resistance. Figure 9(b) shows the corresponding Bode impedance and phase angle plots. It is clear that the impedance modulus and phase angle of S3 alloy are larger than those of S1 and S2 alloys, so as to have large polarization resistance and better corrosion resistance [32,33].

Equivalent circuits as well as fitting data are provided in Figs. 9(c, d), and Table 2. The charge transfer resistance (R_{ct}) and surface film resistance (R_L and R_f) are considered together to evaluate the corrosion resistance, while the solution resistance (R_s) is not considered in the corrosion term, owing to its much smaller resistance [34]. Besides, CPE represents a double-layer capacitor which is defined by Y_0 (corrosion capacitance) and constant n (0−1) [35]. Inductance is described by L, which corresponds to the lower frequency inductance loop. The R_{ct} and R_L of the S2 alloy are both higher than those of the S1 alloy. This reflects that the broken

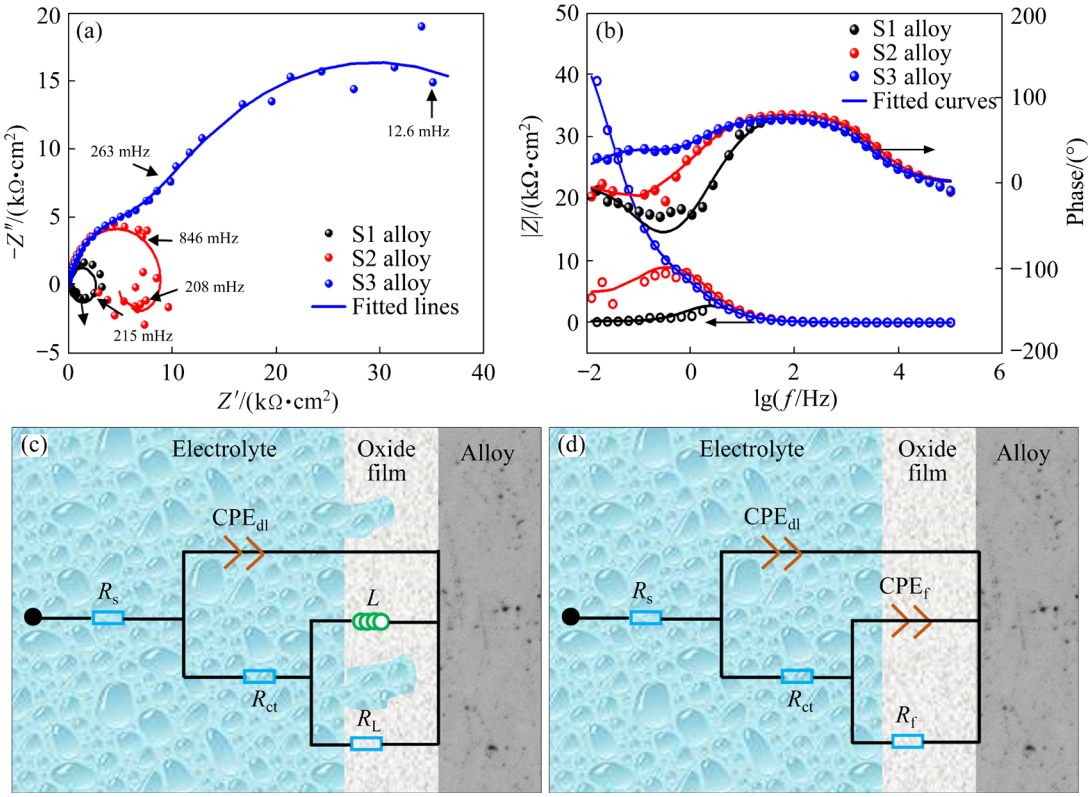

Fig. 9 EIS Nyquist curves (a), Bode phase angle and impedance plots of investigated alloys (b), and equivalent circuits used for fitting EIS of S1, S2 alloys (c), and S3 alloy (d)

oxide film of S1 alloy is more prone to corrosion in the electrolyte. Higher values of R_{ct} (10150 Ω·cm^2) and R_f (42670 Ω·cm^2) represent that the oxide film formed on S3 alloy is more stable than the others, which indicates its better corrosion resistance.

3.4 Microstructure of peak-aged alloys

The evolution of the microstructure of peak-aged alloys is shown in Figs. 10−13. Figure 10 shows the results of grain structure on analysis of EBSD characterization. According to the IPF images (Figs. 10(a−c)) and the corresponding statistical results of grain size, the mean size of recrystallization grains decreases with the shortening of solution heat treatment time. The grain size of the S3 alloy is minimum with a mean size of (7.5±3.8) μm. The segregation and precipitation at GBs will probably be less with smaller grain sizes. In addition, as shown in Figs. 10(d−f), the distribution and frequency histograms of misorientation angle show that the fraction of low angle grain boundaries (LAGBs, 2°−15°) of S3 alloy is 7.8%, which is higher than that of other alloys (S1 alloy: 6.6%, S2 alloy: 6.2%). The higher fraction of LAGBs has an advantage in protecting grain boundaries and improving corrosion resistance [36]. This result also explains the corrosion behavior of S3 alloy as shown in Fig. 7(f), i.e., corrosion is prone to occur and extends along the Al-matrix rather than grain boundaries.

Figure 11 shows the secondary phases and aging precipitates of peak-aged alloys. The SEM images in Figs. 11(a−c) exhibit coarse-scale $Al_6(Mn,Fe)$ phase (black arrows) and fine-scale Al_6Mn phase (yellow arrows), which is similar to the microstructure of as-quenched alloys in Fig. 3. The potential of coarse-scale $Al_6(Mn,Fe)$ phase is more positive than that of Al-matrix (−0.82 V) [37,38], so as to promote the formation of local pit corrosion. The finer Al_6Mn particles can impede the dislocation movement effectively and improve the strength of alloy. The SEM images show no evident difference among the three peak-aged alloys.

Table 2 Fitting results of EIS according to equivalent circuits

Alloy electrode	R_s/(Ω·cm^2)	CPE$_{dl}$		R_{ct}/(Ω·cm^2)	L/H	CPE$_f$		R_f/R_L	χ^2
		Y_0/(10^{-5}Ω^{-1}·cm^2·s^n)	n			Y_0/(10^{-5}Ω^{-1}·cm^2·s^n)	n		
S1	8.30	1.08×10^{-5}	0.95	224	379			2590	6.80×10^{-2}
S2	7.39	1.20×10^{-5}	0.92	4910	6120			4525	1.92×10^{-2}
S3	9.57	1.90×10^{-5}	0.87	10150		9.73×10^{-5}	0.76	42670	2.20×10^{-3}

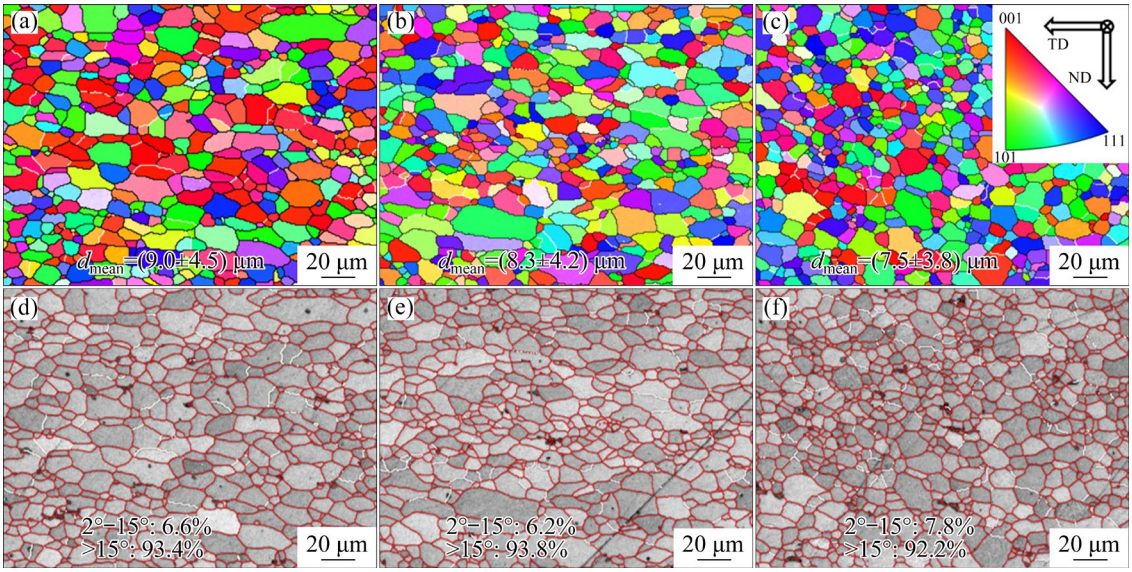

Fig. 10 EBSD results showing grain size (a−c) and misorientation angle (d−f) of different samples: (a, d) S1 alloy; (b, e) S2 alloy; (c, f) S3 alloy

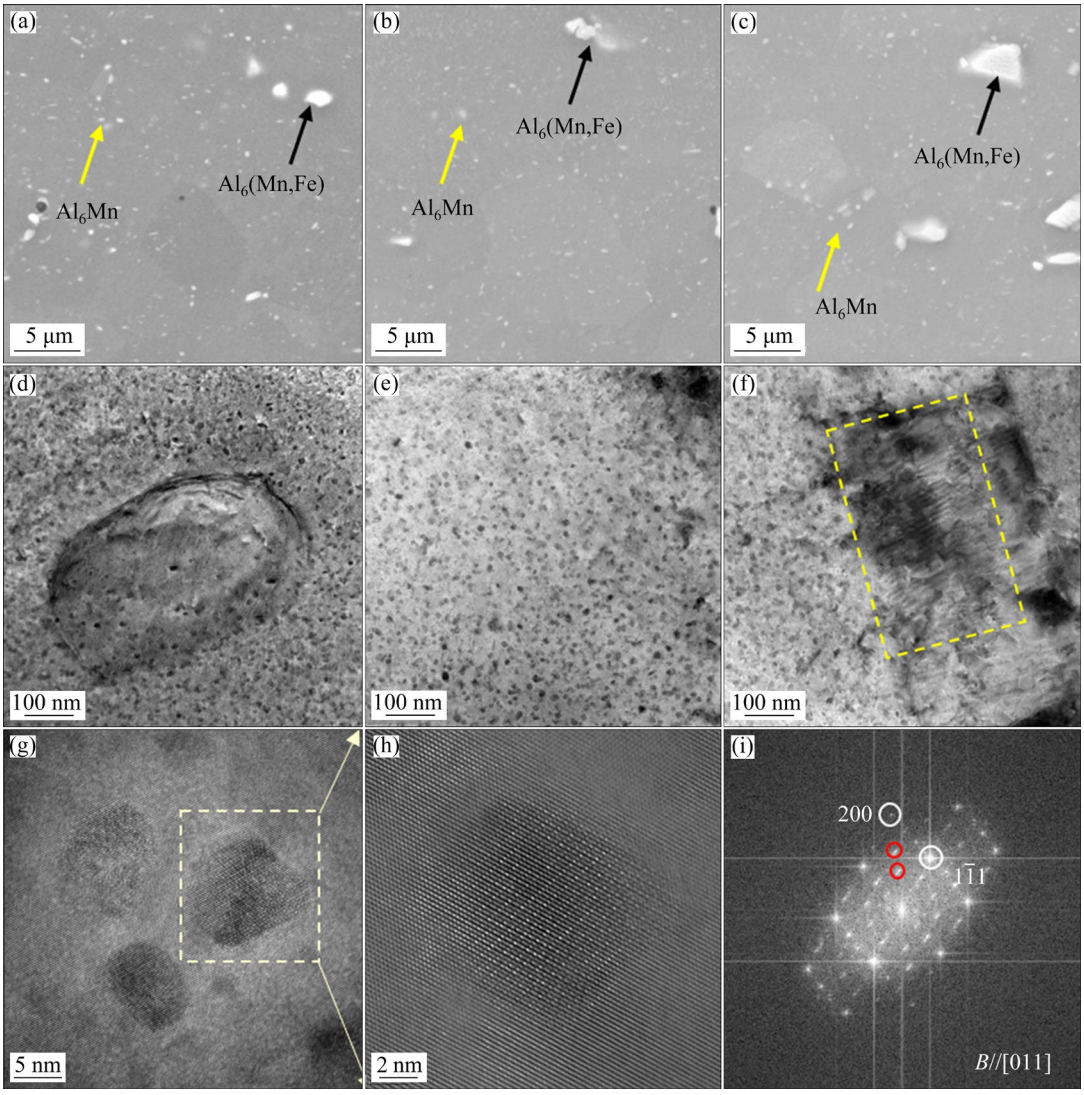

Fig. 11 SEM (a−c) and TEM (d−f) images of S1 alloy (a, d), S2 alloy (b, e) and S3 alloy (c, f), HRTEM image of nano-precipitates (g), enlarged filter image (h), and FFT pattern of nano-particles (i)

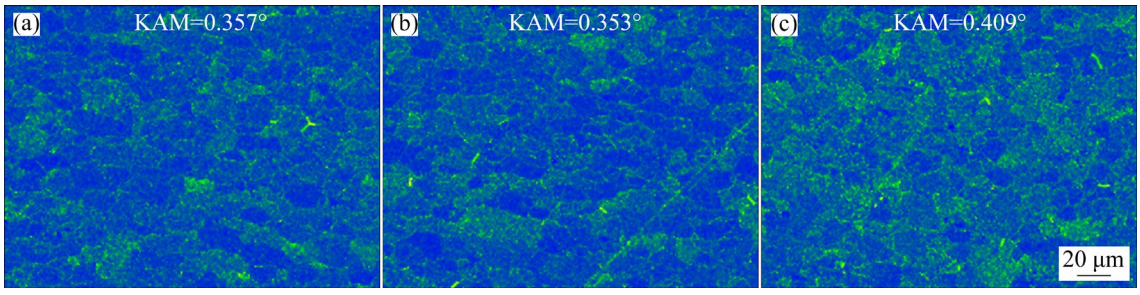

Fig. 12 KAM maps of S1 alloy (a), S2 alloy (b), and S3 alloy (c) based on EBSD results

TEM images in Figs. 11(d−f) present the nano-scale precipitates formed during NIA. Figures 11(g−i) illustrates the HRTEM results and corresponding FFT pattern of the nano-scale particles with a size of about 5 nm. According to the FFT pattern in Fig. 11(i), this particle can be speculated as T'-$Mg_{32}(Al,Zn,Ag)_{49}$ phase (BCC, a=1.41 nm) [39]. Besides, as shown in Fig. 11(h), the precipitate presents a coherent interface with α-Al and can harden the alloy greatly. In addition, a substructure of the dislocation wall which improves the work hardening of the alloy can be observed in

Fig. 11(f) (yellow dashed area). The corresponding kernel average misorientation (KAM) images in Fig. 12 also illustrate that the alloy treated by HTST solution heat treatment can still retain some dislocation structures in the as-aged alloys.

Figure 13 presents the microstructure of grain boundaries and the corresponding EDS results of grain boundary precipitates (GBPs) of investigated alloys. The distribution and composition of GBPs among the peak-aged alloys are similar. Based on the EDS results in Fig. 13(d), in addition to the coarse-scale $Al_6(Mn,Fe)$ phase, some discontinuously distributed GBPs contain the segregation of Mg and Zn elements, which can be determined as T-$Mg_{32}(Al,Zn)_{49}$ phase.

3.5 Mechanical properties

Figure 14 represents the tensile testing results of peak-aged alloys (S1, S2, and S3). The strength is dramatically promoted by HTST solution heat

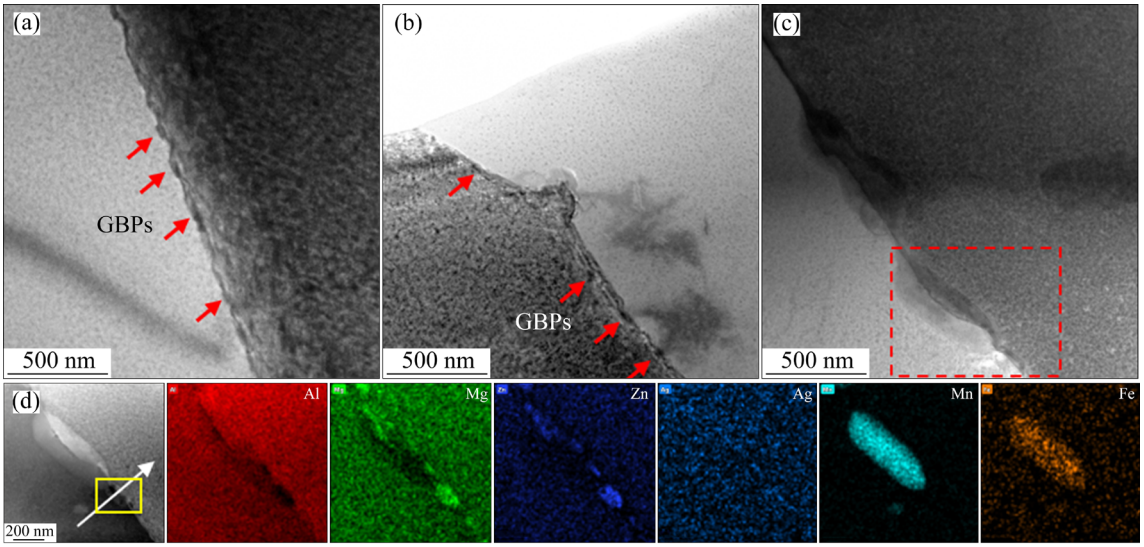

Element	Al	Mg	Zn	Ag	Mn	Fe
Mass fraction/%	83.54	79.53	8.27	1.10	0.38	0.18

Fig. 13 TEM images of grain boundaries of S1 alloy (a), S2 alloy (b) and S3 alloy (c), and enlarged image and EDS results (d) of dashed area in (c)

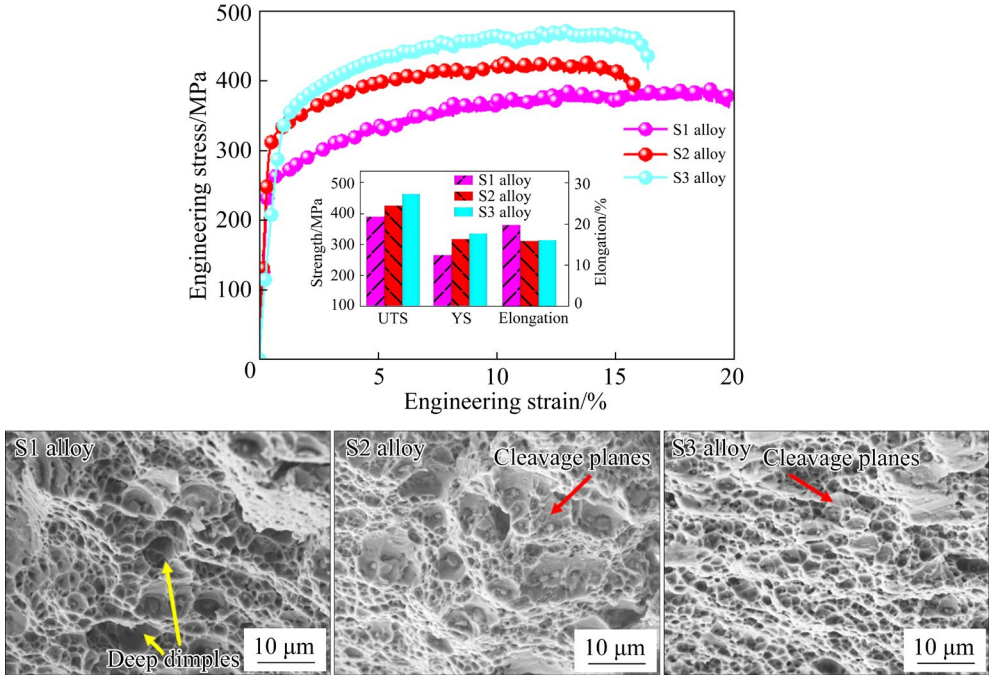

Fig. 14 Mechanical properties and fractographs of investigated alloys

treatment. For S1 alloy, the ultimate tensile strength (UTS) is 390 MPa, and yield strength (YS) is 265 MPa, with an elongation of 19.7%. For the S2 alloy, as the time of solution heat treatment shortens to 30 min, the UTS is 425 MPa, and YS is 317 MPa, with an elongation of 15.8%. The increase in strength can be attributed to the refinement of grains as presented in Fig. 10. The peak hardness of the S2 alloy is lower than that of the S1 alloy, and the S2 alloy represents a higher strength than the S1 alloy. For S3 alloy, the UTS increases to 463 MPa, and YS increases to 335 MPa, with an elongation of 16%. Fractographs of peak-aged alloys after the tensile test are shown in Fig. 14. It is evident that the tensile fracture surface of S1 alloy consists of deep dimples (yellow arrows), which means better ductility of the alloy. However, obvious cleavage planes (red arrows) can be observed on the fracture surfaces of S2 and S3 alloys, thus deteriorating the ductility of alloys.

4 Discussion

4.1 Effect of HTST solution treatment combined with NIA on regulation of as-aged microstructure

For the traditional T6 technology (solution treatment, water quenching, and isothermal aging), the purpose of solution treatment is to promote the dissolution of solute atoms as much as possible, and increase the supersaturation of the alloy combined with the subsequent water quenching [40,41]. Meanwhile, the deformed grains are recrystallized completely, and dislocations are eliminated during solution treatment [42]. However, the microstructure is meliorated by the novel technology of HTST solution treatment combined with NIA in this study. Solution treatment is a process of diffusion phase transformation, and the diffusion coefficient (D) can be expressed as [43]

$$D=D_0\exp[-Q/(RT)] \tag{1}$$

where D_0 is the gas constant; Q is the atomic diffusion constant, R is the molar gas constant (8.314 J/(mol·K)), and T is the thermodynamic temperature.

For HTST solution treatment, the atoms can obtain large amounts of energy and the diffusion of alloy elements can act easily [44,45], which promotes the supersaturation of solid solution [46,47]. More supersaturated atoms and vacancies can increase the precipitation kinetics and nucleation sites greatly. In addition, a shorter heating time of HTST solution treatment is instrumental in restraining the annihilation of dislocations, as shown in Figs. 4(c) and (d).

In the subsequent aging process, compared with isothermal aging, the adopted NIA in this study can promote the precipitation of nano-phase and inhibit the degradation of dislocations at the initial stage with the lower heating temperature. The residual dislocations interact with the precipitates to form a dislocation substructure, as represented in Fig. 11(f). The corresponding KAM maps in Fig. 12 also illustrate the regulation behavior of dislocations by HTST solution treatment combined with NIA.

HTST solution treatment also plays a positive role in inhibiting recrystallization. Recrystallization is a thermal activation process. Avrami equation [48] can be used to describe the recrystallization rate of samples under different solution treatments:

$$X_v=1-\exp[-0.693(t/t_{0.5})^n] \tag{2}$$

$$t_{0.5}=D_1\varepsilon^{a_1}Z^{b_1}\exp[Q_{rec}/(RT_{rec})] \tag{3}$$

where X_v is the recrystallization fraction, t is the annealing time, n and D_1 are the material constants, $t_{0.5}$ is the annealing time required for the recrystallization fraction reaching 50%, Z is the Zener−Hollomon parameter, ε is the prior strain, a_1 and b_1 are constants, Q_{rec} represents the activation energy for recrystallization, and T_{rec} is the holding temperature. Based on the above equation, as the holding temperatures in this study are all much higher than the recrystallization temperature of the alloy, the annealing time has a great influence on the recrystallization fraction of the alloy. This is consistent with the EBSD results in Fig. 10. On the whole, the novel technology of HTST solution treatment combined with NIA can regulate the microstructure such as precipitates, dislocations, and grains effectively, thus improving the properties of the alloy.

4.2 Modification mechanism of mechanical properties and IGC resistance

According to the microstructure above, the increase in the strength of S3 alloy is owing to the combined action of grain boundary strengthening ($\Delta\sigma_{gb}$), precipitation strengthening ($\Delta\sigma_{pre}$), and

dislocation strengthening ($\Delta\sigma_{dis}$). Firstly, grain refinement is an effective method to increase the strength of Al alloys according to the Hall−Petch (HP) equation [49,50]:

$$\Delta\sigma_{gb}=\sigma_0+k_y d^{-1/2} \quad (4)$$

where σ_0 is the yield strength of the matrix, k_y is the HP slope, and d is the grain size. For S3 alloy, the grain refinement caused by HTST solution heat treatment responds to the strength improvement.

The precipitation strengthening mechanism can be explicated by the following equation [51]:

$$\Delta\sigma_{pre}=\frac{Gb}{3d}\sqrt{\frac{f}{2\pi}} \quad (5)$$

where G is the shear modulus, b is the magnitude of Burgers vector, d is the average diameter of precipitates, and f is the volume fraction of precipitates. The more supersaturated atoms and vacancies caused by HTST solution treatment promote the precipitation kinetics and increase the volume fraction of nano-scale T'-$Mg_{32}(Al,Zn,Ag)_{49}$ phase. Besides, as shown in Figs. 4(c) and (d), the alloy processed by HTST solution heat treatment remains some dislocations in the as-quenched microstructure. The residual dislocations serve as nucleation sites to enhance the precipitation of nano-hardening particles during NIA, thus improving the precipitation strengthening response.

Furthermore, as shown in Fig. 11(f), the microstructure of peak-aged S3 alloy includes the dislocation wall substructure, which can enhance the strengthening response of the alloy according to the Bailey−Hirsch equation [52]:

$$\Delta\sigma_{dis}=\alpha MGb\sqrt{\rho} \quad (6)$$

where M is the Taylor factor, α is a constant, and ρ is the dislocation density of the alloy. The higher density of dislocations in S3 alloy contributes to the improvement of the dislocation strengthening effect.

The improvement of IGC resistance by the novel technology of HTST solution treatment combined with NIA can be explained through grain structure and GBPs. Heating temperature and holding time of solution heat treatment determine the recrystallization behavior of grains, so as to influence the size and orientation of the grain. For HTST solution heat treatment, a higher recrystallization temperature increases the nucleation possibility of grains at Al_6(Mn,Fe) phase, so as to enhance the distribution of the Al_6(Mn,Fe) phase along grain boundaries as shown in Fig. 13(c). Meanwhile, short time limits the recrystallization behavior and makes it possible for some deformed grains to maintain a finer scale. Besides, the HTST solution heat treatment remains some deformed dislocations in the as-quenched alloys, as shown in Figs. 4(c) and (d).

During NIA, the movement of dislocations promotes the formation of some substructures. The maintained deformed grains and formed substructures promote the higher fraction of LAGBs in S3 alloy. For another, the residual dislocations provide diffusion channels for solute atoms and inhibit the segregation of GBPs. Therefore, HTST solution heat treatment can not only refine the grain size of as-aged alloys, but also increase the proportion of LAGBs and regulate the distribution of GBPs, hence heightening the corrosion performance of the alloy.

5 Conclusions

(1) The novel technology of HTST solution treatment combined with NIA inhibits the recrystallization behavior, restrains the degradation of dislocations, and promotes precipitation of nano-scale T'-$Mg_{32}(Al,Zn,Ag)_{49}$ phase.

(2) HTST solution heat treatment promotes a higher fraction of LAGBs and increases the noncontinuous distribution of GBPs, which meliorates the corrosion performance of the alloy greatly. The IGC performance of this alloy is improved by the novel technology. The maximum IGC depths of S1, S2 and S3 alloys are 78, 72 and 53 μm, respectively.

(3) HTST solution heat treatment combined with NIA can enhance the strength of Al−Mg−Zn−Ag alloy by the combined mechanism of grain boundary strengthening, precipitation strengthening, and dislocation strengthening. The UTS of S3 alloy is 463 MPa, and the YS is 335 MPa, which are much higher than those of S1 and S2 alloys.

CRediT authorship contribution statement

Cheng GUO: Investigation, Methodology, Writing − Original draft, Funding acquisition; **Yi-fei CHEN** and **Yu-qin GUO:** Investigation, Methodology; **Huan**

WANG: Investigation; **Hai-tao ZHANG:** Conceptualization, Writing − Reviewing and editing; **Jing-qi CHEN:** Methodology, Funding acquisition; **Zi-bin WU:** Investigation; **Xin-gang LIU:** Writing − Reviewing and editing; **Hiromi NAGAUMI:** Conceptualization, Supervision.

Declaration of competing interest

The authors declare that they have no known competing financial interests or personal relationships that could have appeared to influence the work reported in this paper.

Acknowledgments

This research was financially supported by the National Natural Science Foundation of China (Nos. 52204400, 52204401), and the Natural Science Foundation of Hebei Province, China (No. E2022203033).

References

[1] HIRSCH J. Aluminium alloys for automotive application [J]. Materials Science Forum, 1997, 331(242): 33−50.

[2] STEMPER L, TUNES M A, DUMITRASCHKEWITZ P, MENDEZ-MARTIN F, TOSONE R, MARCHAND D, CURTIN W A, UGGOWITZER P J, POGATSCHER S. Giant hardening response in AlMgZn(Cu) alloys [J]. Acta Materialia, 2021, 206: 116617.

[3] HIRSCH J. Recent development in aluminium for automotive applications [J]. Transactions of Nonferrous Metals Society of China, 2014, 24(7): 1995−2002.

[4] HIRSCH J. Aluminium in innovative light-weight car design [J]. Materials Transactions, 2011, 52(5): 818−824.

[5] GUAN L, ZHOU Y, ZHANG B, WANG J Q, HAN E H, KE W. Influence of aging treatment on the pitting behavior associated with the dissolution of active nanoscale β-phase precipitates for an Al−Mg alloy [J]. Corrosion Science, 2016, 103: 255−267.

[6] ZHANG R, ZHANG Y, YAN Y, THOMAS S, DAVIES C H J, BIRBILIS N. The effect of reversion heat treatment on the degree of sensitisation for aluminium alloy AA5083 [J]. Corrosion Science, 2017, 126: 324−333.

[7] ZHU Xin-wen, DENG Ying, LAI Yi, GUO Yi-fan, YANG Zi-ang, FU Le, XU Guo-fu, HUANG Ji-wu. Effects of $Al_3(Sc_{1-x}Zr_x)$ nano-particles on microstructure and mechanical properties of friction-stir-welded Al−Mg−Mn alloys [J]. Transactions of Nonferrous Metals Society of China, 2023, 33(1): 25−35.

[8] HUSKINS E L, CAO B, RAMESH K T. Strengthening mechanisms in an Al−Mg alloy [J]. Materials Science and Engineering: A, 2010, 527(16): 1292−1298.

[9] JI Yuan-yuan, XU Yun-ze, ZHANG Bin-bin, YASHAR B, XIA Da-hai, HU Wen-bin. Review of micro-scale and atomic-scale corrosion mechanisms of second phases in aluminum alloys [J]. Transactions of Nonferrous Metals Society of China, 2021, 31(11): 3205−3227.

[10] LEE B H, KIM S H, PARK J H, KIM H W, LEE J C. Role of Mg in simultaneously improving the strength and ductility of Al−Mg alloys [J]. Materials Science and Engineering: A, 2016, 657: 115−122.

[11] WEN W, ZHAO Y M, MORRIS J G. The effect of Mg precipitation on the mechanical properties of 5xxx aluminum alloys [J]. Materials Science and Engineering: A, 2005, 392 (1/2): 136−144.

[12] MENG C Y, ZHANG D, CUI H, ZHUANG L Z, ZHANG J S. Mechanical properties, intergranular corrosion behavior and microstructure of Zn modified Al−Mg alloys [J]. Journal of Alloys and Compounds, 2014, 617: 925−932.

[13] CAO C, ZHANG D, WANG X, MA Q B, ZHUANG L Z, ZHANG J S. Effects of Cu addition on the precipitation hardening response and intergranular corrosion of Al−5.2Mg−2.0Zn (wt.%) alloy [J]. Materials Characterization, 2016, 122: 177−182.

[14] KUBOTA M, MUDDLE B C. Effect of trace additions of Ag on precipitation in Al−Mg alloys [J]. Materials Transactions, 2005, 46(12): 2968−2974.

[15] HOU S L, LIU P P, ZHANG D, ZHANG J S, ZHUANG L Z. Precipitation hardening behavior and microstructure evolution of Al−5.1Mg−0.15Cu alloy with 3.0 Zn (wt.%) addition [J]. Journal of Materials Science, 2018, 53: 3846−3861.

[16] CAO C, ZHANG D, HE Z B, ZHUANG L Z, ZHANG J S. Enhanced and accelerated age hardening response of Al−5.2Mg−0.45Cu (wt.%) alloy with Zn addition [J]. Materials Science and Engineering: A, 2016, 666: 34−42.

[17] STEMPER L, TUNES M A, OBERHAUSER P, UGGOWITZER P J, POGATSCHER S. Age-hardening response of AlMgZn alloys with Cu and Ag additions [J]. Acta Materialia, 2020, 195: 541−554.

[18] GUO C, ZHANG H T, WU Z B, WANG D T, LI B M, CUI J Z. Effects of Ag on the age hardening response and intergranular corrosion resistance of Al−Mg alloys [J]. Materials Characterization, 2019, 147: 84−92.

[19] GUO C, ZHANG H T, LI S S, CHEN R X, NAN Y F, LI L, WANG P, LI B M, CUI J Z, NAGAUMI H. Evolution of microstructure, mechanical properties and corrosion behavior of Al−4Mg−2Zn−0.3Ag (wt.%) alloy processed by T6 or thermomechanical treatment [J]. Corrosion Science, 2021, 188: 109551.

[20] SO H, SHIN J H, KANG L, JEONG C, KIM K H. Optimization of a solution treatment in the Al−Cu−Mg−Ag alloy via a microstructural investigation [J]. Metals, 2022, 12(1): 66.

[21] GRAF G, SPOERK-ERDELY P, STARON P, STARK A, MENDEZ MARTIN F, CLEMENS H, KLEIN T. Quench rate sensitivity of age-hardenable Al−Zn−Mg−Cu alloys with respect to the Zn/Mg ratio: An in situ SAXS and HEXRD study [J]. Acta Materialia, 2022, 227: 117727.

[22] MILKEREIT B, STARINK M J, ROMETSCH P A, SCHICK C, KESSLER O. Review of the quench sensitivity of aluminium alloys: Analysis of the kinetics and nature of quench-induced precipitation [J]. Materials (Basel, Switzerland), 2019, 12(24): E4083.

[23] GENG Hui-cheng, WANG Yi-lin, ZHU Bin, WANG Zi-jian, ZHANG Yi-sheng. Effect of solution treatment time on

plasticity and ductile fracture of 7075 aluminum alloy sheet in hot stamping process [J]. Transactions of Nonferrous Metals Society of China, 2022, 32(11): 3516−3533.

[24] FARAJOLLAHI R, JAMSHIDI A H, JAMAATI R. Non-isothermal aging behavior of in-situ AA2024−Al_3NiCu composite [J]. Transactions of Nonferrous Metals Society of China, 2022, 32(7): 2125−2137.

[25] PENG X Y, GUO Q, LIANG X P, DENG Y, GU Y, XU G F, YIN Z M. Mechanical properties, corrosion behavior and microstructures of a non-isothermal ageing treated Al−Zn−Mg−Cu alloy [J]. Materials Science and Engineering: A, 2017, 688: 146−154.

[26] ENGLER O, MILLER-JUPP S. Control of second-phase particles in the Al−Mg−Mn alloy AA 5083 [J]. Journal of Alloys and Compounds, 2016, 689: 998−1010.

[27] MOGHANNI-BAVIL-OLYAEI H, ARJOMANDI J, HOSSEINI M. Effects of gallium and lead on the electrochemical behavior of Al−Mg−Sn−Ga−Pb as anode of high rate discharge battery [J]. Journal of Alloys and Compounds, 2017, 695: 2637−2644.

[28] PRAKASHAIAH B G, VINAYA KUMARA D, ANUP PANDITH A, NITYANANDA SHETTY A, AMITHA RANI B E. Corrosion inhibition of 2024-T3 aluminum alloy in 3.5% NaCl by thiosemicarbazone derivatives [J]. Corrosion Science, 2018, 136: 326−338.

[29] CHO Y J, PARK I J, LEE H J, KIM J G. Aluminum anode for aluminum-air battery—Part I: Influence of aluminum purity [J]. Journal of Power Sources, 2015, 277: 370−378.

[30] ZHU C, YANG H X, WU A Q, ZHANG D Q, GAO L X, LIN T. Modified alkaline electrolyte with 8-hydroxyquinoline and ZnO complex additives to improve Al−air battery [J]. Journal of Power Sources, 2019, 432: 55−64.

[31] REN J M, MA J B, ZHANG J, FU C P, SUN B D. Electrochemical performance of pure Al, Al−Sn, Al−Mg and Al−Mg−Sn anodes for Al−air batteries [J]. Journal of Alloys and Compounds, 2019, 808: 151708.

[32] WU P P, XU F J, DENG K K, HAN F Y, ZHANG Z Z, GAO R. Effect of extrusion on corrosion properties of Mg−2Ca−xAl (x=0, 2, 3, 5) alloys [J]. Corrosion Science, 2017, 127: 280−290.

[33] LIU C, BI Q, LEYLAND A, MATTHEWS A. An electrochemical impedance spectropystudy of the corrosion behaviour of PVD coated steels in 0.5N NaCl aqueous solution: Part II. EIS interpretation of corrosion behaviour [J]. Corrosion Science, 2003, 45: 1257−1273.

[34] CHEN J F, FRANKEL G S, JIANG J T, SHAO W Z, ZHEN L. Effect of age-forming on corrosion properties of an Al−Zn−Mg−Cu alloy [J]. Materials and Corrosion, 2014, 65(7): 670−677.

[35] BONORA P L, ANDREI M, ELIEZER A, GUTMAN E M. Corrosion behaviour of stressed magnesium alloys [J]. Corrosion Science, 2002, 44(4): 729−749.

[36] ZHANG X X, JIAO Y B, YU Y, LIU B, HASHIMOTO T, LIU H F, DONG Z H. Intergranular corrosion in AA2024-T3 aluminium alloy: The influence of stored energy and prediction [J]. Corrosion Science, 2019, 155: 1−12.

[37] YASAKAU K A, ZHELUDKEVICH M L, LAMAKA S V, FERREIRA M G S. Role of intermetallic phases in localized corrosion of AA5083 [J]. Electrochimica Acta, 2007, 52 (27): 7651−7659.

[38] TAN L, ALLEN T R. Effect of thermomechanical treatment on the corrosion of AA5083 [J]. Corrosion Science, 2010, 52(2): 548−554.

[39] WANG Y C, WU X D, CAO L F, TONG X, ZOU Y, ZHU Q Q, TANG S B, SONG H, GUO M X. Effect of Ag on aging precipitation behavior and mechanical properties of aluminum alloy 7075 [J]. Materials Science and Engineering A, 2021, 804: 140515.

[40] PENG J, BAHL S, SHYAM A, HAYNES J A, SHIN D. Solute-vacancy clustering in aluminum [J]. Acta Materialia, 2020, 196: 747−758.

[41] MARCEAU R K W, SHA G, FERRAGUT R, DUPASQUIER A, RINGER S P. Solute clustering in Al−Cu−Mg alloys during the early stages of elevated temperature ageing [J]. Acta Materialia, 2010, 58(15): 4923−4939.

[42] LI Z G, ZHANG Z J, ZHOU G W, ZHAO P Z, JIA Z H, POOLE W J. The effect of Mg and Si content on the microstructure, texture and bendability of Al−Mg−Si alloys [J]. Materials Science and Engineering: A, 2021, 814: 141199.

[43] ZHANG Z Q, YU J H, HE D Y. Influence of contact solid-solution treatment on microstructures and mechanical properties of 7075 aluminum alloy [J]. Materials Science and Engineering: A, 2019, 743: 500−503.

[44] JIANG Y B, TANG G Y, SHEK C, LIU W. Microstructure and texture evolution of the cold-rolled AZ91 magnesium alloy strip under electropulsing treatment [J]. Journal of Alloys and Compounds, 2011, 509(11): 4308−4313.

[45] ZHU R F, LIU J N, TANG G Y, SHI S Q, FU M W. Properties, microstructure and texture evolution of cold rolled Cu strips under electropulsing treatment [J]. Journal of Alloys and Compounds, 2012, 544: 203−208.

[46] XU X F, ZHAO Y G, WANG X D, ZHANG Y Y, NING Y H. Effect of rapid solid-solution induced by electropulsing on the microstructure and mechanical properties in 7075 Al alloy [J]. Materials Science and Engineering: A, 2016, 654: 278−281.

[47] PENG G S, CHEN K H, CHEN S Y, FANG H C. Evolution of the second phase particles during the heating-up process of solution treatment of Al−Zn−Mg−Cu alloy [J]. Materials Science and Engineering A, 2015, 641: 237−241.

[48] WELLS M A, SAMARASEKERA I V, BRIMACOMBE J K, HAWBOLT E B, LLOYD D J. Modeling the microstructural changes during hot tandem rolling of AA5xxx aluminum alloys: Part I. Microstructural evolution [J]. Metallurgical and Materials Transactions B, 1998, 29: 611−620.

[49] KENDIG K L, MIRACLE D B. Strengthening mechanisms of an Al−Mg−Sc−Zr alloy [J]. Acta Materialia, 2002, 50(16): 4165−4175.

[50] FANG H J, LIU H, YAN Y, LUO X E, XU X C, CHU X, LU Y J, YU K, WANG D G. Evolution of texture, microstructure, tensile strength and corrosion properties of annealed Al−Mg−Sc−Zr alloys [J]. Materials Science and Engineering: A, 2021, 804: 140682.

[51] YANG Bo-wei, WANG Yu, GAO Min-qiang, WANG Chang-feng, GUAN Ren-guo, Microstructural evolution and strengthening mechanism of Al−Mg alloys with fine grains

processed by accumulative continuous extrusion forming [J]. Journal of Materials Science & Technology, 2022, 128: 195−204.
[52] CHEN Z G, REN J K, YUAN Z G, RINGER S P. Enhanced strength-plasticity combination in an Al−Cu−Mg alloy: Atomic scale microstructure regulation and strengthening mechanisms [J]. Materials Science and Engineering: A, 2020, 787: 139447.

高温短时固溶处理对 Al−Mg−Zn−Ag 合金显微组织与性能的影响

郭 成[1]，陈易飞[1]，郭雨芹[1]，王 欢[1]，张海涛[2]，陈敬琪[1]，吴子彬[3]，刘鑫刚[1]，Hiromi NAGAUMI[3]

1. 燕山大学 机械工程学院，秦皇岛 066004；
2. 东北大学 材料电磁过程研究教育部重点实验室，沈阳 110004；
3. 苏州大学 高性能金属结构材料研究院，苏州 215021

摘 要：将高温短时(HTST)固溶处理与非等温时效(NIA)相结合，对 Al−4.5Mg−2.0Zn−0.3Ag 合金的显微组织与性能进行调控。结果表明，HTST 固溶处理不仅保留了部分变形位错，而且能抑制再结晶行为，增加合金中小角度晶界(LAGBs)的比例。在随后的 NIA 过程中，HTST 固溶处理结合 NIA 有助于抑制位错的退化，同时促进纳米尺度 *T′*-$Mg_{32}(Al,Zn,Ag)_{49}$ 相的析出，进而显著提高合金强度。此外，该新工艺中产生的较高比例 LAGBs 和不连续晶界析出相提高了 Al−4.5Mg−2.0Zn−0.3Ag 合金的耐蚀性。

关键词：Al−Mg−Zn−Ag 合金；固溶处理；非等温时效；显微组织；力学性能；耐蚀性

(Edited by Wei-ping CHEN)